



Lattice Boltzmann simulation of a water droplet penetrating a micropillar array in a microchannel

Cite as: Phys. Fluids **33**, 043308 (2021); <https://doi.org/10.1063/5.0047163>

Submitted: 10 February 2021 . Accepted: 16 March 2021 . Published Online: 08 April 2021

Geng Wang (王耿),  Linlin Fei (费林林), and  Kai H. Luo (罗开红)

COLLECTIONS

Paper published as part of the special topic on [Special Issue on the Lattice Boltzmann Method](#)



View Online



Export Citation



CrossMark

ARTICLES YOU MAY BE INTERESTED IN

[Well-balanced lattice Boltzmann model for two-phase systems](#)

Physics of Fluids **33**, 031709 (2021); <https://doi.org/10.1063/5.0041446>

[Lattice Boltzmann multicomponent model for direct-writing printing](#)

Physics of Fluids **33**, 042103 (2021); <https://doi.org/10.1063/5.0046555>

[Mesoscopic simulation of three-dimensional pool boiling based on a phase-change cascaded lattice Boltzmann method](#)

Physics of Fluids **32**, 103312 (2020); <https://doi.org/10.1063/5.0023639>

Physics of Fluids

SPECIAL TOPIC: Tribute to
Frank M. White on his 88th Anniversary

SUBMIT TODAY!



Lattice Boltzmann simulation of a water droplet penetrating a micropillar array in a microchannel

Cite as: Phys. Fluids **33**, 043308 (2021); doi: [10.1063/5.0047163](https://doi.org/10.1063/5.0047163)

Submitted: 10 February 2021 · Accepted: 16 March 2021 ·

Published Online: 8 April 2021





View Online



Export Citation



CrossMark

Geng Wang (王耿),¹ Linlin Fei (费林林),^{2,a)}  and Kai H. Luo (罗开红),^{1,a)} 

AFFILIATIONS

¹Department of Mechanical Engineering, University College London, Torrington Place, London WC1E 7JE, United Kingdom

²Department of Mechanical and Process Engineering, ETH Zürich (Swiss Federal Institute of Technology in Zürich), Zürich 8092, Switzerland

Note: This paper is part of the Special Issue on the Lattice Boltzmann Method.

^{a)}Authors to whom correspondence should be addressed: linfei@ethz.ch and k.luo@ucl.ac.uk

ABSTRACT

Water droplets penetrating a microchannel equipped with an array of micropillars are commonly seen in engineering applications, ranging from micro-electro-mechanical systems to macro-heat-transfer facilities. Understanding the detailed droplet dynamics in this process is therefore beneficial to the advancement of many fields of industry. In this study, we adopt a nonorthogonal multiple-relaxation-time lattice Boltzmann model to simulate a water droplet penetrating a micropillar array in a microchannel. We first validate our model against the experimental results of (a) off-center impact of a water droplet on a ridged superhydrophobic surface and (b) impact of a water droplet on a curved superhydrophobic surface. Then a comprehensive parametric study is carried out by changing the droplet initial velocity, opening fraction of the micropillar array, and wettability of the micropillar surface. It is found that when the droplet penetrates the micropillar array, its fingering dynamics in the longitudinal direction is governed by the competition between the dynamic and capillary pressures, while the permeation process in the lateral and vertical directions is dominated by the capillary effect. The change of the droplet initial velocity and configuration setup can significantly influence the droplet penetration velocity, maximum wetted surface area, and penetration rate. Finally, a theoretical model is proposed to describe the transient evolution of the droplet penetration mass for a variety of Weber numbers, opening fractions, and static contact angles.

Published under license by AIP Publishing. <https://doi.org/10.1063/5.0047163>

I. INTRODUCTION

In modern engineering, array structures composed of dozens to hundreds of micropillars are extensively employed in the heat transfer equipment^{1–3} and microfluidic devices.^{4,5} For example, a droplet penetrating a microchannel with a micropillar array is ubiquitous during the processes of microdevice cooling,^{3,6,7} phase separation,^{8,9} and microfluidic control.^{4,5} The heat transfer efficiency and mass separation efficiency of the equipment are closely related to the wetted surface area, droplet penetration rate, and penetration time.^{8,9} Besides, those parameters are significantly influenced by the geometry of micropillars and configuration setups.¹⁰ Therefore, gaining an improved understanding of droplet dynamics in such configurations can benefit the design and application of this technique. Although a lot of effort has been made in the past, detailed investigation of droplet dynamics in complex structures is still challenging, especially from a microscale perspective.^{4,8}

Several experimental studies have reported the process of droplet penetrating a microchannel with a micropillar array in advanced

engineering. Two-phase flows in a pin-fin microchannel heat sink have been extensively investigated in Refs. 2, 3, 6, and 7 where the significant influence of droplet entrainment on cooling efficiency was observed. In the studies of Yu *et al.*⁸ and Cheung *et al.*,⁹ a micropillar array was used to separate the liquid phase and gas phase, where various micropillar geometries were tested and compared. Similar configurations have been employed in applications of microfluidic passive control. Link *et al.*¹¹ and Chung *et al.*⁵ experimentally investigated the droplet passive breakup by crossing the microchannel with an array of obstructions. The effects of capillary number, droplet size, and the interval between obstructions have been explored. More outcomes after the droplet passing through the microchannel with an array of obstructions were observed in Refs. 12–14. Owing to the small length scale of this configuration ($10^0 - 10^3 \mu\text{m}$), it is difficult to accurately control the boundary conditions and collect quantitative data due to the experiment limitations.^{7,11} Detailed physical insights into the penetration dynamics, including the evolution of droplet surface area, penetration length, and penetration mass, are currently lacking.

In recent years, numerical simulation techniques have been employed to investigate the droplet dynamics when crossing a microchannel with obstacles. Li *et al.*¹⁵ and Bhardwaj *et al.*¹⁶ have simulated the droplet crossing a microchannel with a partial obstacle by the lattice Boltzmann (LB) method (LBM). In their simulations, the droplet breakup dynamics has been investigated for a variety of capillary numbers and obstruction geometries. Recently, Li *et al.*¹⁷ proposed a three-dimensional diffuse-interface immersed-boundary method to simulate the droplet interaction with complex geometry successfully. Chung *et al.*¹⁸ numerically simulated this configuration by a finite element-front tracking method (FE-FTM). Ma *et al.*¹⁹ and Lee and Son²⁰ numerically investigated the droplet crossing a microchannel with a linear obstacle by volume of fluid (VOF) and level set (LS) method, respectively. In the study of Ma *et al.*,¹⁹ they observed five types of droplet rheological behaviors when crossing the obstacle. And Lee and Son²⁰ suggested that controlling the droplet volume distribution after the breakup can be achieved by varying the obstacle configurations. Chen *et al.*²¹ deployed the LB method to simulate a droplet dripping through microchannels composed of several parallel sheets, and the critical dimensionless numbers governing the droplet deformation phenomena were investigated.

Despite the numerous studies in the field, there is a lack of numerical studies on droplet crossing the microchannel with a micropillar array. Considering the broad applications of such phenomena in advanced engineering, it is desirable to conduct high-fidelity numerical simulations in order to gain further physical insight. Therefore, we adopt an advanced multiple-relaxation-time (MRT) LB model to numerically study a water droplet crossing a micropillar array in a microchannel in this work. The influences of the droplet initial velocity, micropillar geometry, and micropillar surface wettability are systematically investigated. The critical parameters including the droplet penetration mass, penetration length, and surface area evolution are calculated and analyzed in detail. In addition, a theoretical model for predicting the drop penetration rate is constructed. In the Sec. II, the numerical model, computational setup, and model validation are presented. Section III presents the simulation results and discussion. The conclusion of this study is drawn in Sec. IV.

II. METHODOLOGY

A. The lattice Boltzmann multiphase model

Owing to the small scale of the microchannel system, traditional numerical methods based on the continuum fluid assumption may fail in simulating such a configuration.²¹ Alternatively, as a mesoscopic numerical method based on the kinetic theory, the LB method has been broadly employed in simulating complex fluid flow, with scales ranging from microscale to macroscale.^{22,23} In the past few decades,

the LB method has proven its advantages including high parallel efficiency, robust numerical algorithm, and ability to handle complex configurations.²⁴ Specifically for multiphase flow, the interaction between different phases is conveniently described by a pseudopotential,^{25,26} which allows interface deformation, merging, and breakup as well as the specification of physical surface tension. Moreover, the complex microchannel structures can be described with simple boundary treatments including wetting conditions.^{27,28} On the other hand, many LB multiphase models in use suffer from problems such as large spurious velocities, low density ratios, and the dependence of surface tension and density ratio on the viscosity.^{22,24} In the past few years, many efforts have been made to overcome these drawbacks, such as ensuring the mechanical stability, thermodynamic consistency, and decoupling the surface tension and density ratio, as summarized in the comprehensive reviews in Refs. 22 and 29. In this study, we employed an efficient 3D non-orthogonal MRT-LBM³⁰ which incorporates the treatments by Li *et al.*^{25,31} to handle large density ratios and independent surface tension tuning.

In the MRT framework, the collision step is operated in the raw moment space, and the relaxation rates for different moments are adjustable. Compared with the fixed relaxation rate in the single relaxation time (SRT) LB scheme, the MRT framework provides better numerical stability. In particular, the adopted non-orthogonal MRT-LB model has a much lower spurious velocity compared with the SRT-LBM,³⁰ which allows simulation of liquid-gas flow at a significantly larger density ratio. The collision step of the MRT Boltzmann model can be written as³⁰

$$f_i^*(\mathbf{x}, t) = f_i(\mathbf{x}, t) - \Lambda [f_i - f_i^{eq}]_{(\mathbf{x}, t)} + \frac{\Delta t}{2} [\bar{F}_i(\mathbf{x}, t) + \bar{F}_i(\mathbf{x} + \mathbf{e}_i \Delta t, t + \Delta t)], \quad (1)$$

f_i and f_i^* indicate the discrete distribution functions before and after the collision, respectively. \mathbf{x} stands for the position vector, \mathbf{e}_i are the discrete velocities and t is the time. The equilibrium distribution functions f_i^{eq} are given as

$$f_i^{eq} = \rho \omega(|\mathbf{e}_i|^2) \left[1 + \frac{\mathbf{e}_i \cdot \mathbf{u}}{c_s^2} + \frac{(\mathbf{e}_i \cdot \mathbf{u})^2}{2c_s^4} - \frac{(\mathbf{u} \cdot \mathbf{u})}{2c_s^2} \right], \quad (2)$$

where ρ stands for density, the lattice sound speed $c_s = 1/\sqrt{3}$, and $\mathbf{u} = [u_x, u_y, u_z]$ demonstrates fluid velocity. The D3Q19 lattice model is adopted in this study, and its weights are $\omega(0) = 1/3$, $\omega(1) = 1/18$, and $\omega(2) = 1/36$. The discrete velocities $\mathbf{e}_i = [e_{ix}, e_{iy}, e_{iz}]$ are described as

$$\begin{aligned} |e_{iy}\rangle &= [0, 1, -1, 0, 0, 0, 0, 1, -1, 1, -1, 1, -1, 0, 0, 0, 0, 1, -1, 1, -1, 1, -1, 1, -1]^T, \\ |e_{iy}\rangle &= [0, 0, 0, 1, -1, 0, 0, 1, 1, -1, -1, 0, 0, 0, 0, 1, -1, 1, -1, 1, 1, -1, -1, 1, 1, -1]^T, \\ |e_{iz}\rangle &= [0, 0, 0, 0, 0, 0, 1, -1, 0, 0, 0, 0, 1, 1, -1, -1, 1, 1, -1, -1, 1, 1, 1, -1, -1, -1]^T, \end{aligned}$$

where $i = 0, 1, \dots, 18$, $|\cdot\rangle$ denotes a 19-dimensional column vector, and the superscript T represents the transposition. The forcing terms \bar{F}_i in Eq. (1) are written as³²

$$\bar{F}_i = \omega(|\mathbf{e}_i|^2) \left[\frac{\mathbf{e}_i \cdot \mathbf{u}}{c_s^2} + \frac{(\mathbf{e}_i \cdot \mathbf{u}) \mathbf{e}_i}{c_s^4} \right] \cdot \mathbf{F}, \quad (3)$$

$\mathbf{F} = [F_x, F_y, F_z]$ is the total force imposed on the fluid. The pseudopotential model is utilized to simulate the multiphase flow, and the interactions between the liquid phase and gas phase are represented by a pseudopotential force²⁶

$$\mathbf{F}_{int} = -G\psi(\mathbf{x}) \sum_i w(|\mathbf{e}_i|^2) \psi(\mathbf{x} + \mathbf{e}_i \Delta t) \mathbf{e}_i, \quad (4)$$

where the interaction strength G is usually set as -1 , ψ is the pseudopotential, and the weights are $w(|\mathbf{e}_i|^2) = \omega(|\mathbf{e}_i|^2)/c_s^2$. To simulate the large density ratio multiphase flow, the square-root-form pseudopotential $\psi = \sqrt{2(P_{EOS} - \rho c_s^2)/Gc^2}$ is applied in this work,^{34,35} where $c = 1$ is the lattice constant and P_{EOS} is the pressure in the equation of state. In addition, the following term is incorporated into \bar{F}_i (i.e., $\mathbf{F} = \mathbf{F}_{int} + \mathbf{F}_{ads}$) to describe the interaction between the fluid and a solid matrix.²⁸

$$\mathbf{F}_{ads} = -G_{ads}\psi(\mathbf{x}) \sum_i w(|\mathbf{e}_i|^2) \psi(\mathbf{x}) s(\mathbf{x} + \mathbf{e}_i \Delta t) \mathbf{e}_i, \quad (5)$$

where G_{ads} is the fluid-solid interaction strength to adjust the contact angle. $s(\mathbf{x})$ is an indicator function which equals 1 for solid and 0 for fluid, respectively. For simplification, the static contact angle is adopted during the simulation. It has been proved that this treatment is able to simulate the droplet dynamics for a wide range of surface wettability when the inertia effect plays an important role.³⁰ For cases where the capillarity is dominant, the contact angle hysteresis should be included via more advanced methods, e.g., the geometric formulation.^{36,37}

The collision operator Λ in Eq. (1) equals $\mathbf{M}^{-1}\mathbf{S}\mathbf{M}$, where \mathbf{S} is a diagonal relaxation matrix and \mathbf{M} is the transformation matrix. In 2014, Lycett-Brown and Luo³⁸ initially constructed an MRT-LBM based on a non-orthogonal transformation matrix and demonstrated its improved stability compared to the classical SRT-LBM for 2D problems. Recently, Li *et al.*³⁹ further showed that a 3D nonorthogonal MRT-LBM can retain numerical accuracy while simplifying the implementation compared with its orthogonal counterpart. Based on a generalized multiple-relaxation-time scheme,^{33,40} Fei *et al.* proposed another nonorthogonal MRT-LBM which is compatible with different discrete velocity models.³⁰ In this work, we employ the approach of the non-orthogonal transformation matrix proposed by Fei *et al.*³⁰ Compared with the classical MRT model, this implementation has been proved to be more efficient and exhibits better portability across different lattice models.^{30,41} Multiplication of the explicit form of Eq. (1) by the transformation matrix \mathbf{M} [given in Eq. (C4) in Ref. 30] leads to the collision equation in the moment space as follows:³⁰

$$\bar{\mathbf{m}}^* = \bar{\mathbf{m}} - S(\bar{\mathbf{m}} - \mathbf{m}^{eq}) + \left(\mathbf{I} - \frac{\mathbf{S}}{2} \right) \Delta t \bar{\mathbf{F}}, \quad (6)$$

where \mathbf{I} is the unit matrix, the transformation $\bar{f}_i = f_i - \Delta t \bar{F}_i/2$ has been used to remove the implicit scheme in Eq. (1), $\bar{\mathbf{m}} = \mathbf{M}\bar{\mathbf{f}}$, $\mathbf{m}^{eq} = \mathbf{M}\mathbf{f}^{eq}$, and $\bar{\mathbf{F}} = \mathbf{M}\bar{\mathbf{F}}$. The equilibrium moments can be obtained

$$\begin{aligned} \mathbf{m}^{eq} = & [\rho, \rho u_x, \rho u_y, \rho u_z, \rho u_x u_y, \rho u_x u_z, \rho u_y u_z, \rho(1 + \mathbf{u}^2), \\ & \rho(u_x^2 - u_y^2), \rho(u_x^2 - u_z^2), \rho c_s^2 u_x, \rho c_s^2 u_y, \rho c_s^2 u_z, \\ & \rho c_s^2 u_y, \rho c_s^2 u_z, \rho c_s^2 (c_s^2 + u_x^2 + u_y^2), \rho c_s^2 (c_s^2 + u_x^2 + u_z^2), \\ & \rho c_s^2 (c_s^2 + u_y^2 + u_z^2)]^T. \end{aligned} \quad (7)$$

Similarly, the forcing terms in the moment space are given as

$$\begin{aligned} \bar{\mathbf{F}} = & [0, F_x, F_y, F_z, F_x u_y + F_y u_x, F_x u_z + F_z u_x, F_y u_z + F_z u_y, \\ & 2\mathbf{F} \cdot \mathbf{u}, 2(F_x u_x - F_y u_y), 2(F_x u_x - F_z u_z), F_x c_s^2, F_x c_s^2, F_y c_s^2, \\ & F_z c_s^2, F_y c_s^2, F_z c_s^2, 2c_s^2(F_x u_x + F_y u_y), 2c_s^2(F_x u_x + F_z u_z), \\ & 2c_s^2(F_y u_y + F_z u_z)]^T. \end{aligned} \quad (8)$$

Besides, the diagonal relaxation matrix \mathbf{S} is defined as

$$\mathbf{S} = \text{diag}(s_0, s_1, s_1, s_1, s_2, s_2, s_2, s_2b, s_2, s_2, s_3, s_3, s_3, s_3, s_3, s_3, s_4, s_4, s_4). \quad (9)$$

The kinematic and bulk viscosities are calculated by $\nu = (1/S_2 - 0.5)C_s^2\Delta t$ and $\zeta = 2/3(1/s_{2b} - 0.5)C_s^2\Delta t$, respectively.

The tunable surface tension and thermodynamic consistency are obtained via modifying some elements in the forcing terms³⁰

$$\begin{aligned} \bar{F}'_4 = & \bar{F}_4 - \frac{Q_{xy}}{(s_2^{-1} - 0.5)\Delta t}, \quad \bar{F}'_5 = \bar{F}_5 - \frac{Q_{xz}}{(s_2^{-1} - 0.5)\Delta t}, \\ \bar{F}'_6 = & \bar{F}_6 - \frac{Q_{yz}}{(s_2^{-1} - 0.5)\Delta t}, \\ \bar{F}'_7 = & \bar{F}_7 + \frac{6\sigma|\mathbf{F}_{int}|^2}{\psi^2(s_{2b}^{-1} - 0.5)\Delta t} + \frac{4(Q_{xx} + Q_{yy} + Q_{zz})}{5(s_{2b}^{-1} - 0.5)\Delta t}, \\ \bar{F}'_8 = & \bar{F}_8 - \frac{(Q_{xx} - Q_{yy})}{(s_2^{-1} - 0.5)\Delta t}, \quad \bar{F}'_9 = \bar{F}_9 - \frac{(Q_{xx} - Q_{zz})}{(s_2^{-1} - 0.5)\Delta t}, \end{aligned}$$

where the tunable parameter σ restores the thermodynamic consistency. The variable $Q_{\alpha\beta}$ is given by³¹

$$Q_{\alpha\beta} = \kappa \frac{G}{2} \psi(\mathbf{x}) \sum_i w(|\mathbf{e}_i|^2) [\psi(\mathbf{x} + \mathbf{e}_i \Delta t) - \psi(\mathbf{x})] e_{i\alpha} e_{i\beta}, \quad (10)$$

where the parameter κ is used to tune the surface tension (γ). Following the collision step, the discrete distribution functions are reconstructed by $\bar{f}_i^* = \mathbf{M}^{-1}\bar{\mathbf{m}}^*$. By streaming from the present position \mathbf{x} to the neighboring positions ($\mathbf{x} + \mathbf{e}_i \Delta t$) along the discrete velocity directions, the updated discrete distribution functions are

$$\bar{f}_i(\mathbf{x} + \mathbf{e}_i \Delta t, t + \Delta t) = \bar{f}_i^*(\mathbf{x}, t). \quad (11)$$

The fluid properties in the physical space can be calculated by

$$\rho = \sum_i \bar{f}_i, \quad \rho \mathbf{u} = \sum_i \bar{f}_i \mathbf{e}_i + \frac{\Delta t \mathbf{F}}{2}. \quad (12)$$

The introduced model has been widely adopted to simulate multiphase flow at large density ratios.^{30,41,42}

B. Model validation

We first conducted a contact angle validation by simulating the dynamic wetting process of a water droplet with a radius $R_0 = 35$, and G_{ads} is changed from -0.12 to 0.25 . To eliminate the influence of the interface width, the droplet is initially placed two lattices away from the plate. After the droplet reaches a steady state, the static contact angle (θ) can be calculated by the relation $\tan(\theta/2) = 2h/l$, where h is the droplet height. The transient evolution of contact line length (l) is plotted as a function of dimensionless time ($t^* = t/\tau$, the inertia-capillarity time $\tau = (R_0^3 \rho_l/\gamma)^{0.5}$) in Fig. 1(a). From the figure, we can

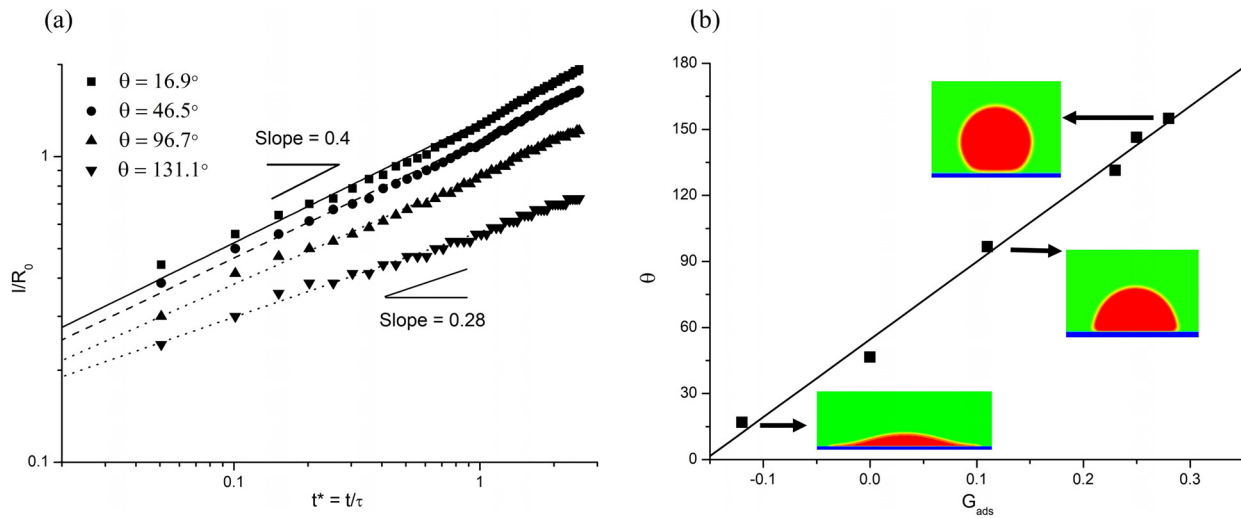


FIG. 1. (a) A log-log plot of the transient evolution of contact line length as a function of dimensionless time. The lines in the figure are the fitted curves $l/R_0 = C \cdot (t/\tau)^n$. (b) The static contact angle θ vs G_{ads} .

find that the contact length evolution follows a power law $l \sim t^n$ in all cases. And the slope of the best fitting functions [lines in Fig. 1(a)] decreases with the increase of the static contact angle and ranges from 0.28 to 0.4, which is in line with the findings in Ref. 43. The relation between G_{ads} and θ is plotted at Fig. 1(b). It is noticed that θ has approximately a linear relation with G_{ads} . However, there is no analytical relation between the specified contact angle and the value of G_{ads} , and G_{ads} needs to be tuned to match the prescribed contact angle.

We then validate our numerical models against the experimental study⁴⁴ of a water droplet off-center impacting on a single-ridge superhydrophobic surface. In the experiment, the initial diameter of the water droplet (D_0) is 2.84 mm, the measured static contact angle (θ) of the surface is $160 \pm 1^\circ$, and the ridge width and height are 1.0 mm and 1.5 mm, respectively. The impact Weber number defined based on the impacting velocity V_0 ($We = D_0 V_0^2 \rho / \gamma$) is kept as 15.2, and the dimensionless off-centered distance ($e^* = e/D_0$, where e is the distance between the vertical centerline of the droplet and single ridge) varies from 0.16 to 0.54.

In our simulations, the droplet radius is fixed at 50 lattice units, the corresponding ridge width and height are 35 and 53, respectively. G_{ads} is set to be 0.3 to achieve the experimental wetting condition ($\theta = 160^\circ$). Under the lattice units, the liquid density (ρ) is 1, droplet kinematic viscosity (ν) is 0.0025, and droplet surface tension (γ) is 0.01. To match the experimental conditions, the density ratio and the kinematic viscosity ratio between the liquid phase and the gas phase are kept at 1000 and 20, respectively. With the Weber number $We = 15.8 \pm 0.3$, we have Ohnesorge number $Oh = (\rho\nu) / \sqrt{\gamma\rho D_0} < 0.004$ in the simulation. By changing the position of the droplet, we achieve three cases considered in the experiments, namely, e^* equal to 0.16, 0.33, and 0.54, respectively.

Figure 2 presents the simulated dynamic process of the droplet interacting with the ridge. In line with the experimental results,⁴⁴ the three different off-center distances lead to different impacting dynamics and outcomes, namely: (a) Type 1, the droplet passes over the ridge and asymmetrically breaks up into two droplets; one satellite droplet

stays behind the ridge and the other goes in front of the ridge; Type 2, the droplet bumps on the ridge and gets significantly deformed; a small part of the droplet separates from the rest and sits on top of the ridge; and Type 3, the droplet smashes onto the ridge; its head goes over the ridge temporarily but retreats back behind the ridge. For all three cases, the LB simulations reproduce all the dynamic features of the initial droplet and its satellite droplets. Only small discrepancies are observed in the fine details in the simulated and photographed droplets, which may be attributed to different lighting or coloring effects.

Further validation is conducted by simulating a water droplet of radius $R_0 = 1.45$ mm impacting a curved superhydrophobic surface, and the simulation results are compared with the experimental results in Ref. 45. The droplet initial radius is fixed as 50 lattice units. Consistent with the experiment, the impacting We is set as 15.8, and the diameter ratio between the curved surface and the droplet is approximately 2.8. In this case, G_{ads} is set as 0.28, the corresponding static contact angle is 155° , ν is 0.005, and $Oh < 0.005$. The evolution of the droplet as well as the variations of the contact line length (normalized by the droplet initial diameter) in the axial and azimuthal directions is shown in Fig. 3. As shown in Fig. 3, the simulation results are both quantitatively and qualitatively in agreement with the experimental results. Some small differences occur at the contact line length in the azimuthal direction when the droplet retracts, which may be due to the differences in measuring the curved contact length between the experiment and simulation.

C. Simulation setups

Figure 4(a) shows the three-dimensional (3D) physical configuration of the droplet and a microchannel with a micropillar array assembly, and Fig. 4(b) gives the two-dimensional top view. The micropillar array is equipped with 5 micropillars in the lateral direction and 6 rows of staggered micropillars in the longitudinal direction. The height (vertical) and width (lateral) of the microchannel are the same as the

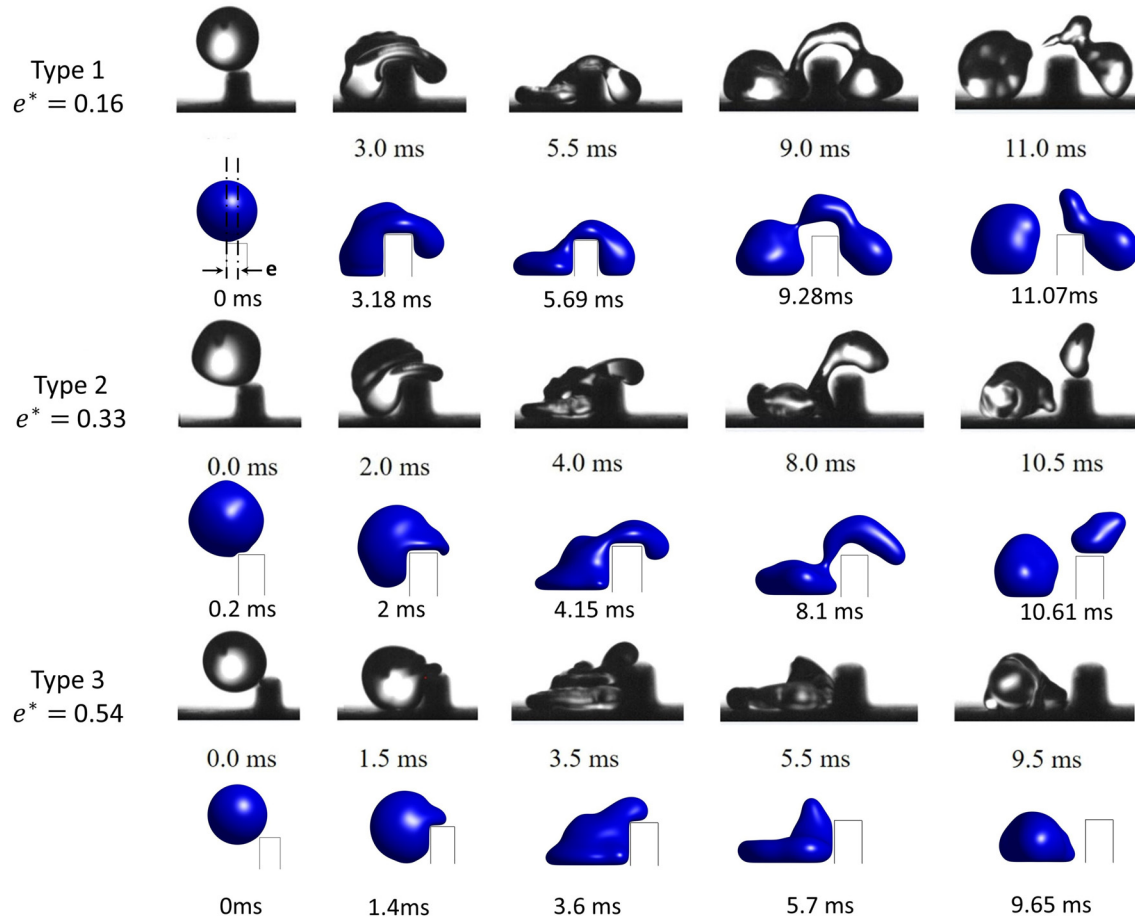


FIG. 2. Comparison between the experimental snapshots (gray)⁴⁴ and the LB simulation (blue) results of a water droplet off-center impacting on a single-ridge surface at $We = 15.2$. Three different sets of droplet outcomes are observed for three different off-centered distances (e^*).

width of the micropillar array; the length (longitudinal) of the microchannel is equal to the length of the micropillar array plus 4.5 times the initial droplet diameter.

The center of the droplet is aligned with the centerline of the microchannel in the longitudinal direction, and the droplet initial diameter and velocity are D_0 and V_0 , respectively. As expressed in Fig. 4(b), the distances between the center of two micropillars in the longitudinal direction (L_s) and the lateral direction (W) are fixed as $0.5 D_0$ and $0.4 D_0$, respectively. The opening fractions of the pillar array in the lateral direction ($\phi_{la} = (W - W_p) / W$) and in the longitudinal direction ($\phi_{lo} = (L_s - L_p) / L_s$) are tuned by changing the width (W_p) and length (L_p) of micropillars, respectively. In this study, periodic boundary conditions are imposed in the longitudinal directions, and the non-slip boundary condition is imposed at the microchannel walls as well as the micropillar array surfaces. For simplicity, the walls and the array surfaces have the same wettability.

A mesh independence study is first conducted by simulating the same configuration on successively finer grids. The initial diameter and velocity of the water droplet are 0.5 mm and 1.1 m/s, respectively. The static contact angle of the micropillar surface (θ) is 46.5° ; ϕ_{la} and ϕ_{lo} are both fixed as 0.5. The droplet radius (R) is refined gradually,

from 45, 55, 70 to 90 lattices, which leads to the final mesh number in the lateral (N_{la}), vertical (N_v), and longitudinal (N_{lo}) directions, $N_{la} \times N_v \times N_{lo} = 180 \times 180 \times 652$, $220 \times 220 \times 798$, $280 \times 280 \times 1015$, and $360 \times 360 \times 1305$, respectively. All the other parameters are kept the same. Figure 5 presents the time evolution of the droplet penetration mass, where the time and mass are normalized by the inertial-capillarity time τ and droplet initial mass M_0 , respectively ($t^* = 0$ denotes the time when the droplet first touches with the micropillar array). As we can see, the cases $dx = R/45$ and $dx = R/55$ deviate from other cases apparently, indicating insufficient grid resolutions. For the cases when $dx \leq R/70$, the differences are negligible. Therefore, in the following simulations, 70 grid points are used for the droplet radius, giving over 20 grid points for the distance between micropillars, and this setup leads to the total grid points of over 75×10^6 for the following cases.

III. RESULTS AND DISCUSSION

To systematically investigate the droplet dynamics when it penetrates a micropillar array in a microchannel, a comprehensive parametric study is carried out by varying the droplet initial velocity (V_0), micropillar array opening fraction (ϕ_{la} and ϕ_{lo}) and micropillar

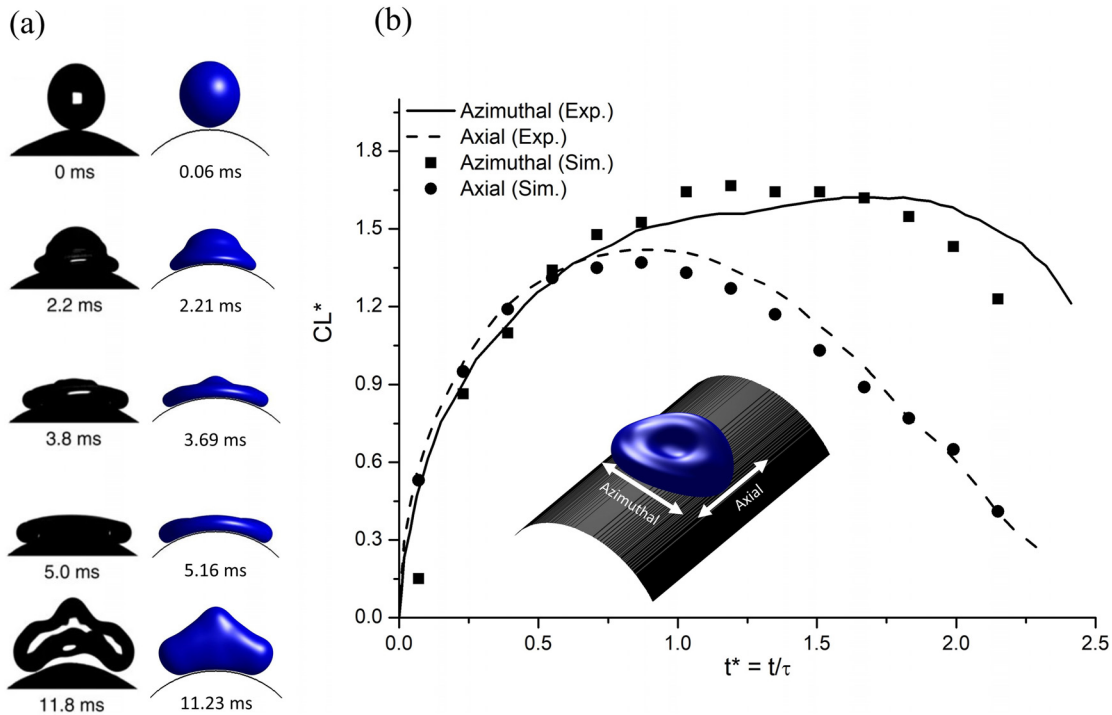


FIG. 3. (a) Simulation snapshots (blue) and experiment images (gray) for a droplet impact on a curved superhydrophobic surface; (b) comparison of the normalized contact line length in the axial and azimuthal directions obtained by experiment (lines) and simulation (symbols).

surface wettability (θ). In the following simulations, the water droplet radius is kept as 0.25 mm. Owing to the droplet diameter far less than the capillary length $L_c = 2.7$ mm, the effect of gravity is negligible.⁴⁶ Under the lattice units, the droplet initial radius equals 70, ν is 0.005 and $Oh < 0.005$ for all cases. All the other setups are kept as the same as Sec. II C.

A. Influences of droplet initial velocity

In this section, we simulate the introduced water droplet with four different initial velocities, $V_0 = 0.3$ m/s, 0.5 m/s, 1.1 m/s, and

2 m/s, giving the impacting We as 0.62, 1.72, 8.3, and 27.5, respectively. The opening fraction of the micropillar array $\phi_{la} = \phi_{lo} = 0.5$, and the measured static contact angle of the micropillar surface (θ) is set as 46.5° . Figure 6 presents the droplet evolution process at $We = 0.62, 8.3,$ and 27.5 , respectively. As indicated in the figure, when the droplet touches the micropillar array, driven by the inertia force, it penetrates rapidly in the longitudinal direction as a finger shape and permeates slower in the lateral and vertical directions. For the higher We cases, owing to a higher inertia pressure, its penetration velocity is significantly higher, and therefore its penetration length in the longitudinal direction (L) is longer at the same time instant. In the meantime, for

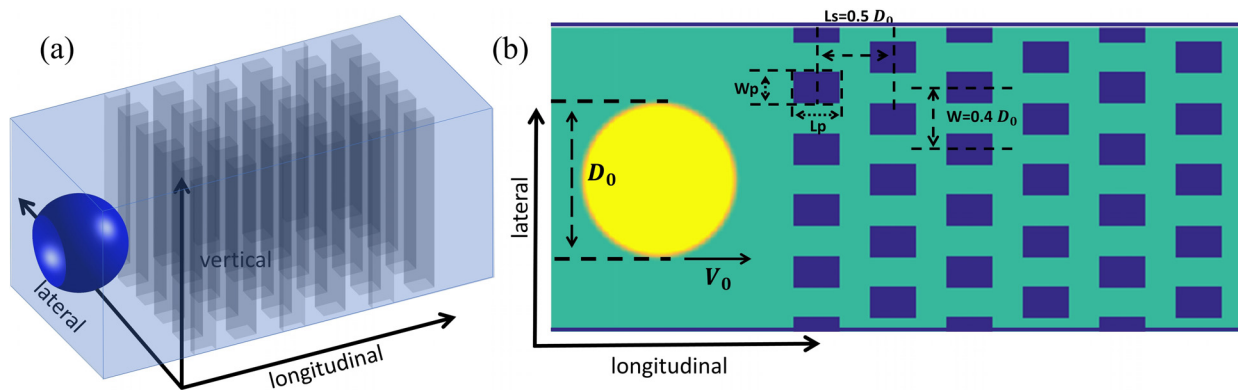


FIG. 4. The 3D main view (a) and 2D top view (b) of a water droplet and a microchannel with a micropillar array assembly.

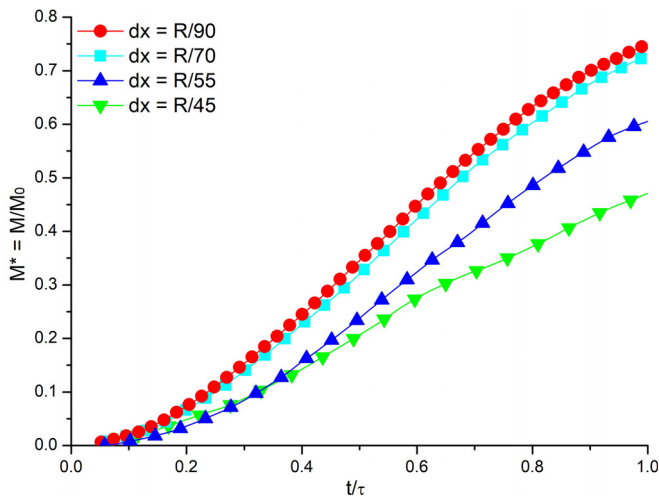


FIG. 5. The variation of the droplet penetration mass in the micropillar array for various droplet radius resolutions.

the higher We cases, the droplet permeates wider in both the lateral and vertical directions and finally leads to a higher wetted surface area ($S = S_{liquid-gas} + S_{liquid-solid}$, where $S_{liquid-solid}$ is the contact area between the liquid phase and solid phase, and $S_{liquid-gas}$ is the interface area between the liquid and gas phases).

The findings regarding the wetted surface area can be explained by the balance of the droplet energy: owing to the small magnitude of Oh (<0.005), the influence of the viscous force can be ignored compared with the inertial force and surface tension.⁴⁷ When the droplet touches the micropillar array, its kinetic energy ($KE = 0.5\rho V_0^2$) is converted into the surface free energy ($SE = \gamma S_{liquid-gas} + \gamma_{liquid-solid} S_{liquid-solid}$, where $\gamma_{liquid-solid}$ is the liquid-solid interfacial energy).^{42,48} As a result, a higher V_0 indicates a higher KE and finally leads to a higher SE and S .

Additionally, for the case at $We = 27.5$, it can be observed the liquid necklace inside the micropillar further breaks up into satellite droplets, as has also been captured in Ref. 49. A video for this case $We = 8.3$ is provided in the supplementary material movie 1.

The transient evolution of droplet penetration length and wetted surface area is then recorded and analyzed. The dimensionless penetration length ($L^* = L/D_0$) and wetted surface area ($S^* = S/S_0$, where S_0 is the droplet initial surface area) vs t^* are plotted in Figs. 7(a) and 7(b), respectively. As shown in Fig. 7(a), for the droplet at $We = 27.5$, its penetration length increases the fastest, which concurs with the qualitative results in Fig. 6. The penetration length evolutions for the lower We ($We = 0.62$ and $We = 1.72$) cases almost coincide. Furthermore, we can find during the whole evolution process ($t^* = 0 - 2$) that the penetration length generally increases linearly. To make it clear, the development of droplet penetration length in the first row of micropillars ($L/D_0 < 0.5$) has also been plotted in the inset of Fig. 7(a). During this period, for the cases with higher We ($We > 10^1$), inertia is regarded as the dominant effect and therefore the penetration velocity is increased with V_0 [see dotted line and dashed-dotted line in the inset of Fig. 7(a)]. For the cases at lower We ($We \sim 10^0$), as introduced in Refs. 50 and 51, the development of the penetration length follows a constant velocity at the very initial period [see solid line and dashed line in the inset of Fig. 7(a)]. In Fig. 7(a), some small “steps” (stops of penetration) can be found during the evolution, which implies the permeation of the droplet in lateral and vertical directions. Regarding the evolution of S^* , as demonstrated in Fig. 7(b), it first reaches a maximum value then decreases owing to the droplet retraction as well as a part of the droplet going out of the micropillar array. As expected, the maximum value of S increases with We , which is consistent with the results in Fig. 6 and the previous energy analysis.

Figures 8(a) and 8(b) express the dimensionless droplet penetration mass ($M^* = M/M_0$) inside the micropillar array vs t^* . For each case, the penetration mass first increases to a peak value and then decreases. Likewise, for the higher We case, the penetration mass accumulates more quickly. To further explore the evolution of droplet

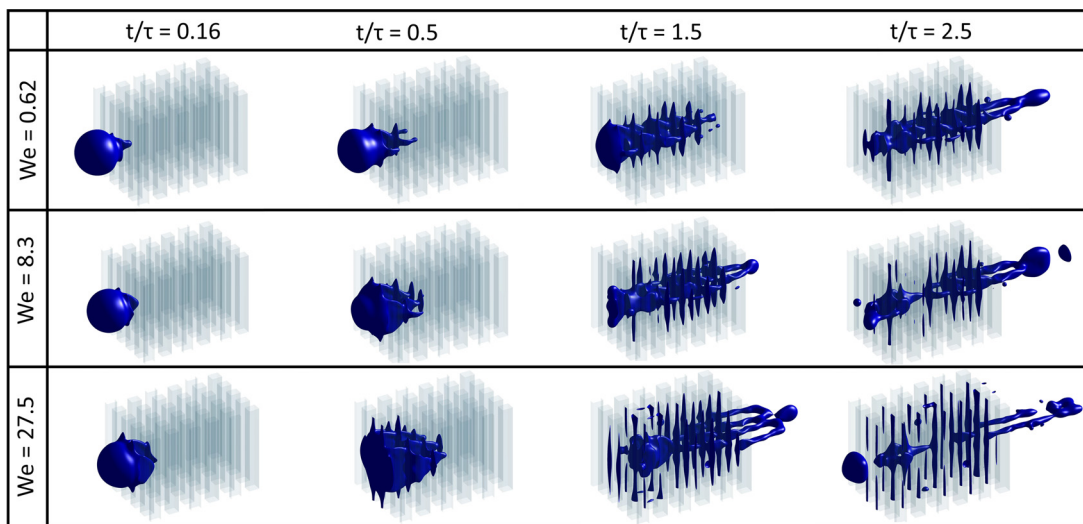


FIG. 6. 3D main view of the droplet evolution in the micropillar array with different Weber numbers at $\phi_{la} = \phi_{lo} = 0.5$ and $\theta = 46.5^\circ$.

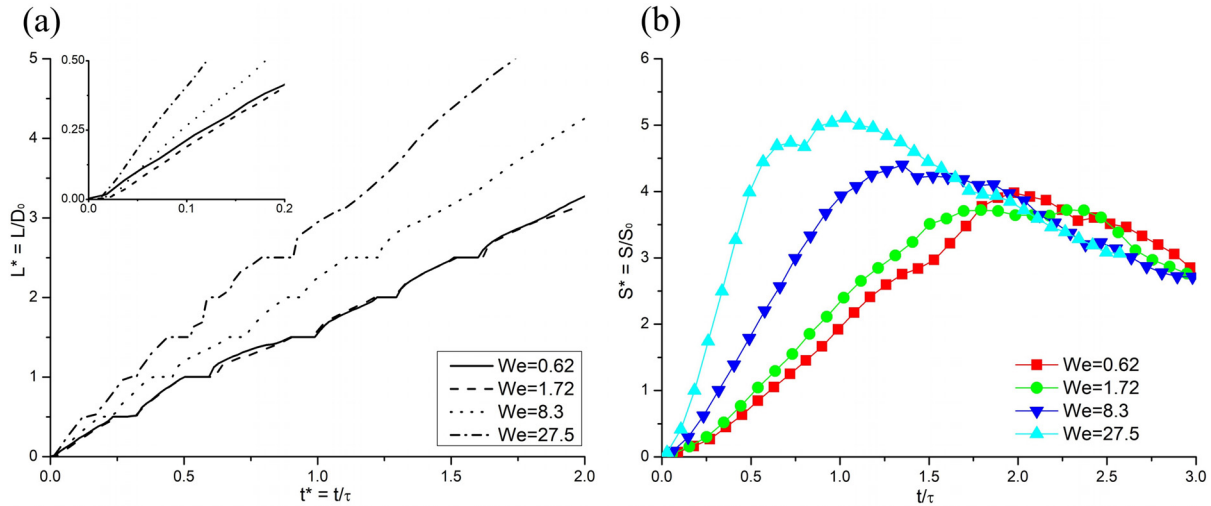


FIG. 7. For various We cases, at $\phi_{la} = \phi_{lo} = 0.5$ and $\theta = 46.5^\circ$, (a) the dimensionless droplet penetration length and (b) wetted surface area as a function of dimensionless time. The inset figure of (a) denotes the development of droplet penetration length in the first row of micropillars ($L/D_0 < 0.5$).

penetration mass, we plot the droplet penetration mass during the infiltration stage (shaded area in Fig. 8(a), $t^* < 1.25$) in a log-log axis. As demonstrated in Fig. 8(b), during this stage, the evolution of penetration mass follows a power-law fitting. More interestingly, the exponent of the fitting lines is almost the same, independent of We . The power-law dependency of the penetration mass is in line with the previous findings for a droplet impacting a porous medium.^{52,53} In the following, we will propose a new model to describe the evolution of droplet penetration mass. As the analysis of Fig. 7(a), the droplet penetration length (L) in the longitudinal direction can be regarded as a linear dependency, and the competition of the dynamic pressure and the capillary pressure determines the penetration velocity. So, L scales as

$$L \sim \left(\sqrt{V_0^2 + \frac{4\gamma\cos(\theta_f)}{\rho D_{\max}}} \right) t, \quad (13)$$

where the term in the bracket is the approximate penetration velocity (V_p), and it is achieved through the balance of the dynamic pressure and capillary pressure before ($0.5\rho V_0^2$) and after ($0.5\rho V_p^2 + F(\theta_f)$) droplet impact. The capillary term $F(\theta_f)$ approximates $-2\gamma\cos(\theta_f)/D_{\max}$. The maximum spread diameter D_{\max} approximates $2D_0$, which is a typical value when droplet impacting orifice structure for the Weber number within the current range.⁵⁴ It should be mentioned that we ignored the capillary effect in the lateral direction because of a very short period of the droplet and micropillar interaction [see the

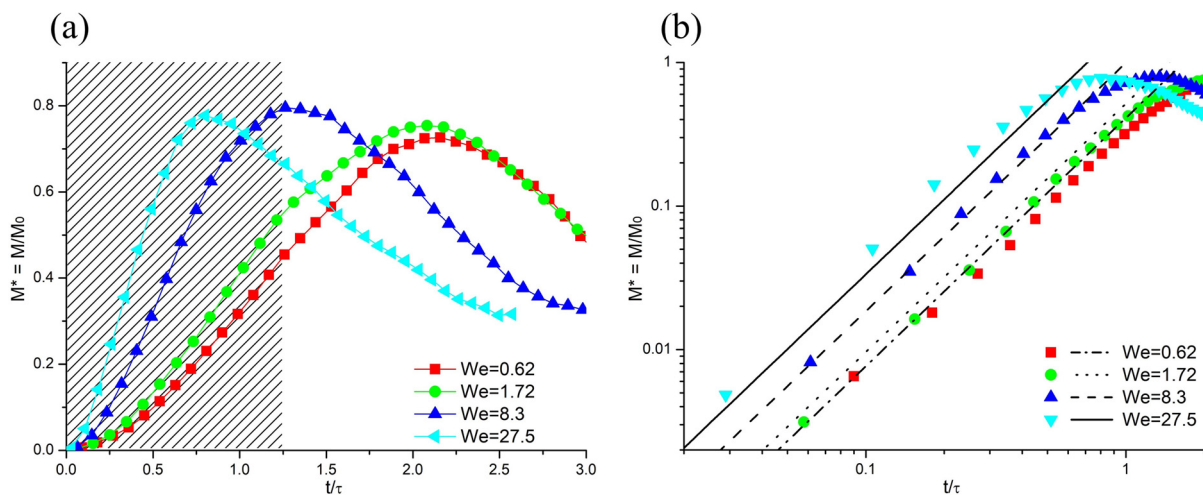


FIG. 8. (a) The dimensionless droplet penetration mass of the whole simulation period and (b) droplet infiltration stage for various We cases, at $\phi_{la} = \phi_{lo} = 0.5$ and $\theta = 46.5^\circ$. The shadowed area in (a) represents the droplet infiltration stage, and lines in (b) stand for Eq. (17).

inset of Fig. 7(a)].⁵⁵ Following Refs. 51 and 56, we calculate θ_f by the relation

$$\theta_f^3 = 9ACa + \theta^3, \tag{14}$$

where constant $A = 14$ and capillary number $Ca = \phi_{la} \cdot \rho \nu V_0 / \gamma$.

For the permeation of the droplet in the lateral and vertical directions, owing to the small inertia pressure in these two directions, it can be assumed that the capillary effect is dominant. Gardner⁵⁷ proposed that the rise of liquid capillary length in a uniform radius (r) capillary tube follows $(\gamma w \cos(\theta_f) t / (2\rho \nu))^{0.5}$. However, it cannot be directly extended when the geometry varies in the different directions.^{52,58} As an alternative, we adopted the theory in Ref. 58, where the permeation length of the droplet in the lateral and vertical directions can be scaled as

$$L_{l,v} \sim \left(\frac{\gamma \cos(\theta_f)}{4\rho \nu w^{1-2D_T}} \right)^{\frac{1}{2D_T}} (t)^{\frac{1}{2D_T}}, \tag{15}$$

where the subscripts of L represent the directions, D_T is related to the geometry, and $1 < D_T < 3$.⁵⁸ The approximate opening width w in Eq. (15) is chosen as the opening width in the longitudinal and vertical directions $w = 0.4\phi_{la}D_0$, which are the main directions of the droplet permeation (see in Fig. 5). Meanwhile, the effect of the opening width in the lateral direction is ignored. The approximate dynamic contact angle (θ_f) in Eq. (15) is chosen as a constant value $\cong 50^\circ$, which is the typical value of the front contact angle in a low velocity region.^{51,59} Substituting the dimensionless number We and eliminating all the constant terms, M^* could be given as a scale of

$$M^* \sim LL_l L_v \sim (We + 2 \cdot \cos(\theta_f))^{0.5} \cdot \phi_{la}^{1-\frac{1}{2D_T}} \cdot (t^*)^{1+\frac{1}{2D_T}}. \tag{16}$$

In this study, we choose $D_T = 1.37$, and the best-fitted equation is

$$M^* = 0.54 \cdot (We + 2 \cdot \cos(\theta_f))^{0.5} \cdot \phi_{la}^{0.635} \cdot (t^*)^{1.73}. \tag{17}$$

Equation (17) is plotted as lines in Fig. 8(b), where we can see the proposed model agrees well with our simulation results over a wide range of t^* for different We cases. The penetration rates for simulation results at $We = 0.62$ and $We = 1.72$ are slightly lower than the theoretical one, possibly because the capillary effect term in Eq. (13) is overestimated at a low We . In the following, this model be further validated under a wider range of key parameters (ϕ_{la} and θ).

B. Influences of the micropillar geometry

In this section, we will further explore the effects of micropillar geometry. We simulate the same penetration case as in Sec. III A, where the droplet penetrates a micropillar array with $\theta = 46.5^\circ$, at $V_0 = 1.1$ m/s (corresponding to $We = 8.3$). By varying W_p and L_p , ϕ_{la} and ϕ_{lo} are changed from 0.15 to 0.85. The corresponding opening width of the micropillar array in the physical unit varies from $38 \mu\text{m}$ to $220 \mu\text{m}$. The evolution of the droplet is plotted in Fig. 9. The first and second rows stand for the micropillar array with the same ϕ_{la} and different ϕ_{lo} , and the second and the third rows denote the micropillar array with the same ϕ_{lo} and different ϕ_{la} . A video for the case with $\phi_{la} = 0.31$ and $\phi_{lo} = 0.7$ is provided in the supplementary material movie 2. Qualitatively, we can find for the same ϕ_{la} cases, a higher ϕ_{lo} , that the droplet has a longer penetration length at the same time point. For the same ϕ_{lo} cases, the development of penetration length is slower for the lower ϕ_{la} case. As a result, we can find that more liquid penetrates throughout the micropillar array at $t/\tau = 2.2$ for the higher ϕ_{lo} and ϕ_{la} cases.

The detailed evolution of droplet penetration length (L) is plotted in Figs. 10(a) and 10(b). As we can find in Fig. 10(a), for the cases with a fixed $\phi_{lo} = 0.5$ and different ϕ_{la} , the droplet presents the longest penetration time for the lowest ϕ_{la} during the whole evolution period. The reason is that a lower ϕ_{la} leads more liquid to permeate in the

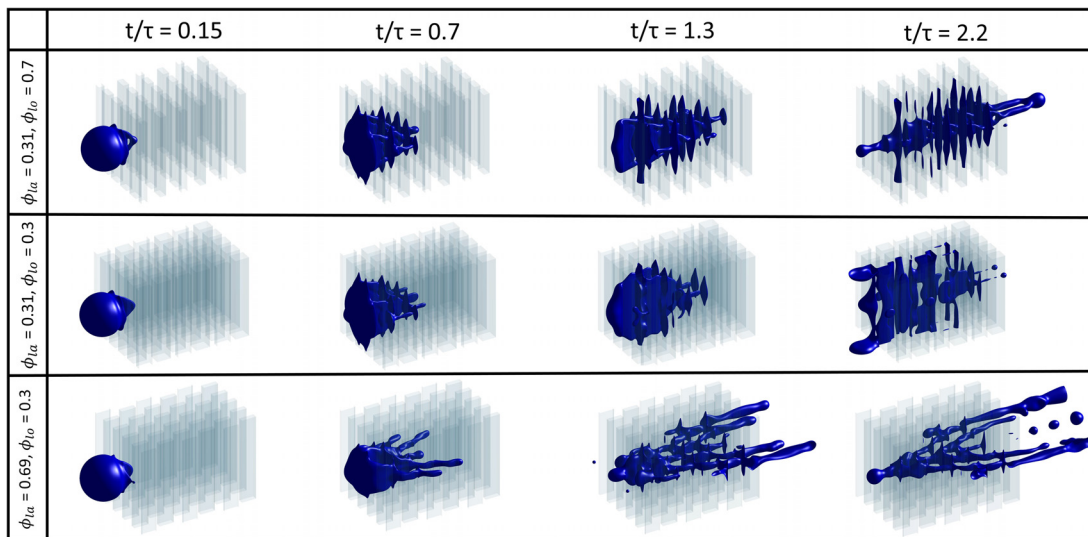


FIG. 9. 3D main view of the droplet evolution in the micropillar array at different ϕ_{la} and ϕ_{lo} , with $We = 8.3$ and $\theta = 46.5^\circ$. The rows in the figure represent different ϕ_{la} and ϕ_{lo} cases, and the columns indicate time series.

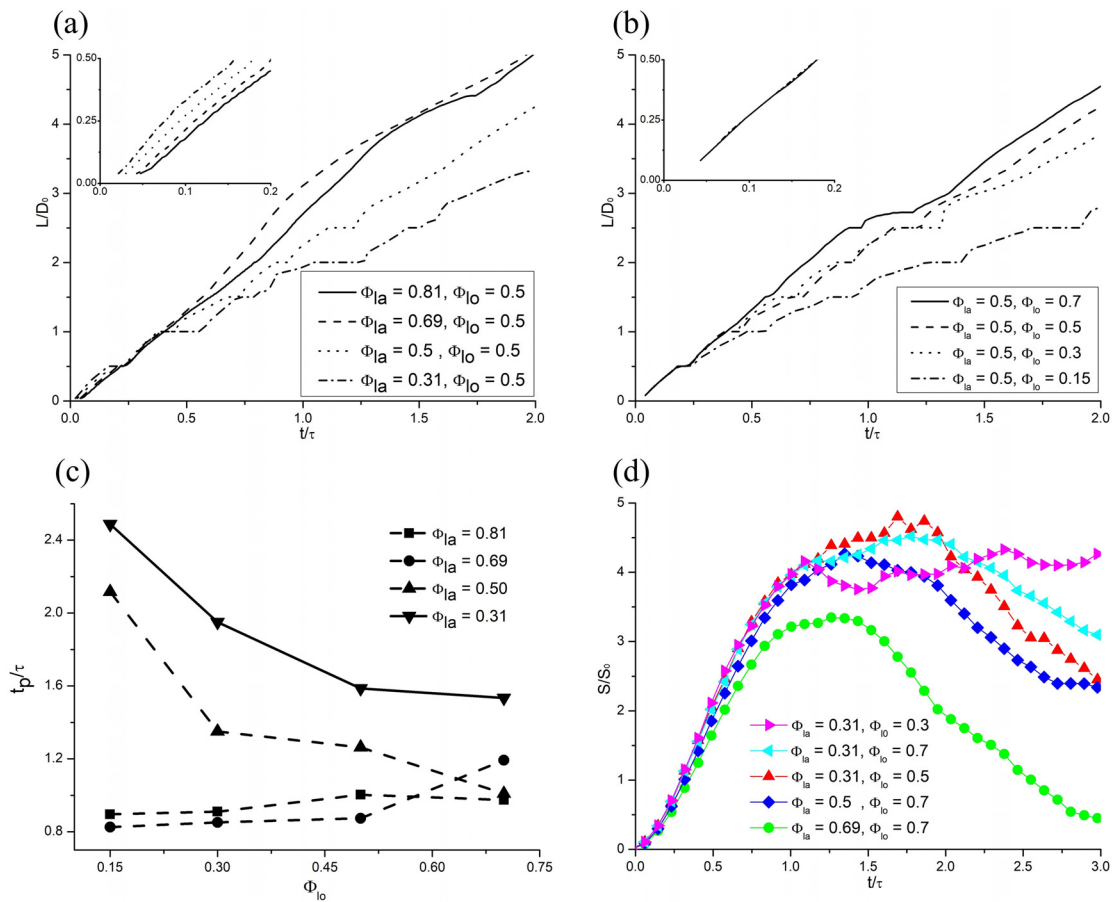


FIG. 10. For the cases of various ϕ_{la} and ϕ_{lo} , at $We = 8.3$ and $\theta = 46.5^\circ$. The dimensionless droplet penetration length vs the dimensionless time for (a) $\phi_{lo} = 0.5$ cases and (b) $\phi_{la} = 0.5$ cases. The inset figures of (a) and (b) denote the variation of droplet penetration length in the first row of micropillars ($L/D_0 < 0.5$). (c) indicates the droplet penetration time and (d) represents the wetted surface area vs the dimensionless time.

lateral and vertical directions; therefore, we can find more significant “steps” during the evolution process [see the dashed and dotted lines in Fig. 10(a)]. The permeation of the droplet in the lateral and vertical directions decreases the inertia effect in the longitudinal direction, which results in a lower penetration velocity. In contrast, for the droplet penetration in the first row of the micropillar array ($L/D_0 < 0.5$), as indicated in the inset of Fig. 10(a), a lower ϕ_{la} experiences a higher penetration velocity when only considering the capillary and inertia force. Moreover, it can be found that the length evolutions for $\phi_{la} = 0.69$ and $\phi_{la} = 0.81$ cases are similar because the inertial effect plays a role when the lateral opening fraction is very wide. For the cases with a fixed $\phi_{la} = 0.5$ and different ϕ_{lo} , as shown in Fig. 10(b), it can be found that for the highest ϕ_{lo} cases, the droplet penetrates the fastest. And we can see in the inset of Fig. 10(b), ϕ_{lo} has no influence on the penetration velocity when the droplet crosses a parallel micropillar because the inertia and surface tension forces are all the same during this period.

We also recorded the penetration time $t_p = t_{out} - t_{in}$ when the droplet crosses the micropillar array, where t_{in} and t_{out} are the time instants when the liquid first touches the inlet and outlet of the micropillar array, respectively. The dimensionless penetration time

($t_p^* = t_p/\tau$) for different ϕ_{la} and ϕ_{lo} is plotted in Fig. 10(c). As we can see, for the lowest ϕ_{la} cases, the droplet penetration time is the longest, and the penetration time significantly decreases with the increase in ϕ_{lo} . For the higher ϕ_{la} cases, the droplet penetration time is shorter because of the dominance of the inertial effect, and the variation of ϕ_{lo} has little influence on the penetration time. Figure 10(d) presents the evolution of S^* , as shown in the figure, for the cases with the same ϕ_{la} [triangle symbols in Fig. 10(d)], the droplet spread rate is similar. For the highest ϕ_{la} case, the maximum value of S is the lowest and decreases the fastest.

Similar to Sec. III A, we recorded the penetration mass of the droplet and plotted it in Fig. 11. Figure 11(a) shows the variation of droplet penetration mass for different ϕ_{la} and ϕ_{lo} cases. As we can find, the droplet penetration mass first increases to a peak value and then decreases. And the penetration rate is increased with ϕ_{la} , consistent with the trends of the penetration length. Moreover, we can see for the higher ϕ_{la} cases, the droplet penetration mass decreases rapidly after reaching the peak value, indicating droplet leaves the micropillar array. Such a finding concurs with our results in Fig. 10(c). It can be also observed that the penetration rates for the same ϕ_{la} but different ϕ_{lo} cases are the same, which is because the penetration of the droplet

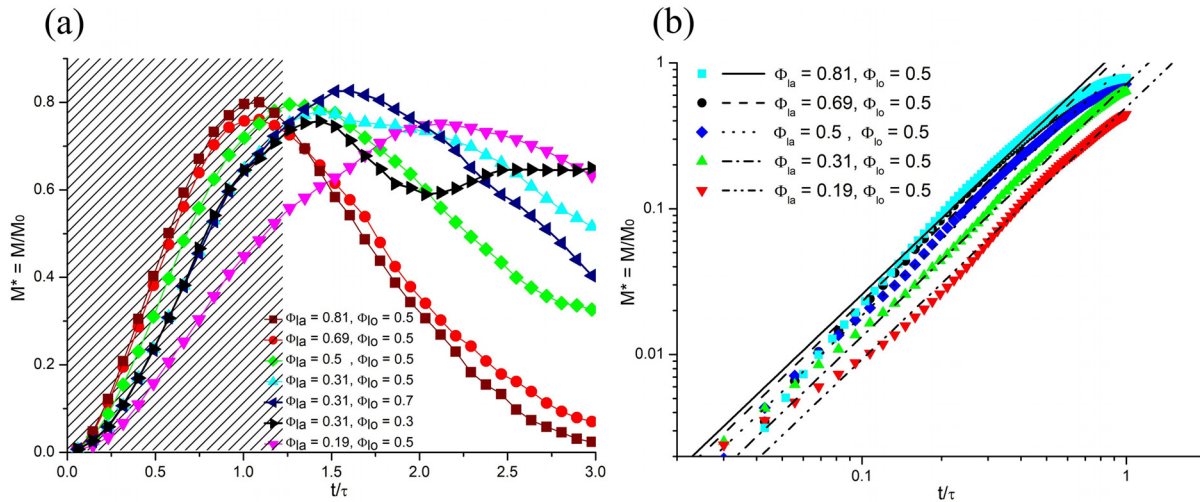


FIG. 11. (a) Transient evolution of droplet penetration mass during the whole simulation period for different ϕ_{la} and ϕ_{lo} cases, at $We = 8.3$ and $\theta = 46.5^\circ$. (b) The development of droplet penetration mass during the infiltration stage for $\phi_{lo} = 0.5$. The shadowed area in (a) represents the droplet infiltration stage, and lines in (b) stand for Eq. (17).

concentrates on the longitudinal and vertical directions. This finding also validates Eq. (15). The droplet penetration mass for different ϕ_{la} in the infiltration stage and Eq. (17) is plotted in Fig. 11(b). As shown in the figure, our proposed model also agrees exactly with the LB simulation results at various of ϕ_{la} . Some deviations occur at the very beginning ($t^* < 0.08$), which is due to a different dynamic mechanism for droplet capillary penetration at this stage.^{51,60}

C. Influences of the micropillar surface wettability

Finally, the influences of the micropillar surface wettability will be explored. In the following study, we simulate the same 0.25 mm radius water droplet penetrating a micropillar array with different θ .

We consider four cases with $\theta = 16.9^\circ, 46.5^\circ, 96.7^\circ$, and 131.3° , respectively. The opening fractions of the micropillar array are set as $\phi_{la} = \phi_{lo} = 0.5$, the droplet V_0 is kept as 1.1 m/s and the corresponding We is equal to 8.3. Figure 12 shows the droplet evolution at $\theta = 16.9^\circ, 96.7^\circ$, and 131.3° , and a video for the case with $\theta = 96.7^\circ$ is provided in the supplementary material movie 3. As shown in the figure, the penetration rate is faster for the lower θ cases, which is in line with the results in Ref. 52. Likewise, for the lower θ cases, its wetted surface area (S) is significantly higher. The mechanism can be interpreted by referring to the Young's equation ($\cos(\theta) = (\gamma_{gas-solid} - \gamma_{liquid-solid}) / \gamma$, where $\gamma_{gas-solid}$ is the gas-solid interfacial energy) and surface energy equation ($SE = \gamma S_{liquid-gas} + \gamma_{liquid-solid} S_{liquid-solid}$). For the same converted SE, assuming all the other parameters are the same, a lower

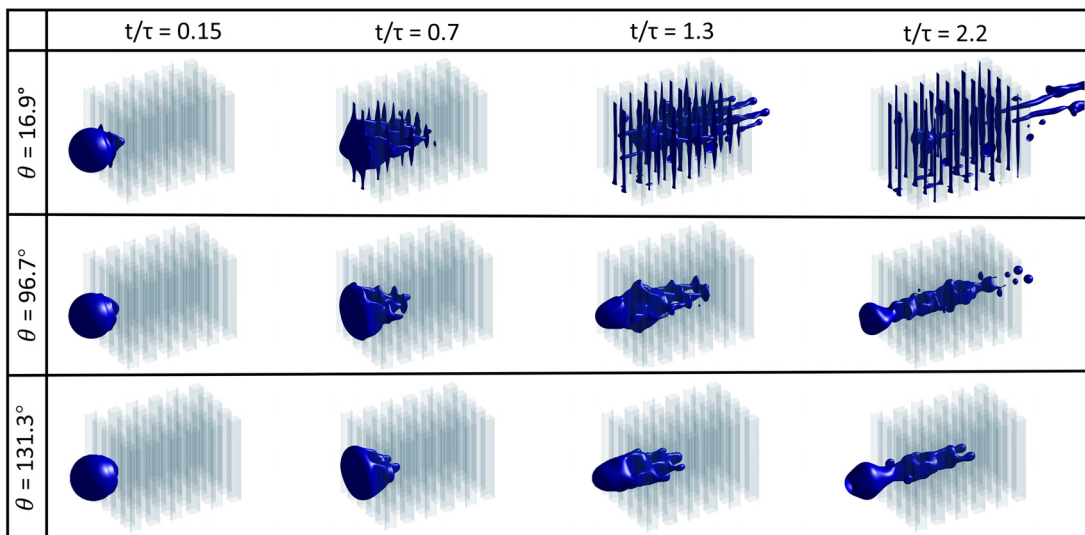


FIG. 12. 3D main view of the droplet evolution in the micropillar array with different θ at $We = 8.3$ and $\phi_{la} = \phi_{lo} = 0.5$. The rows in the figure represent different θ cases, and the columns indicate time series.

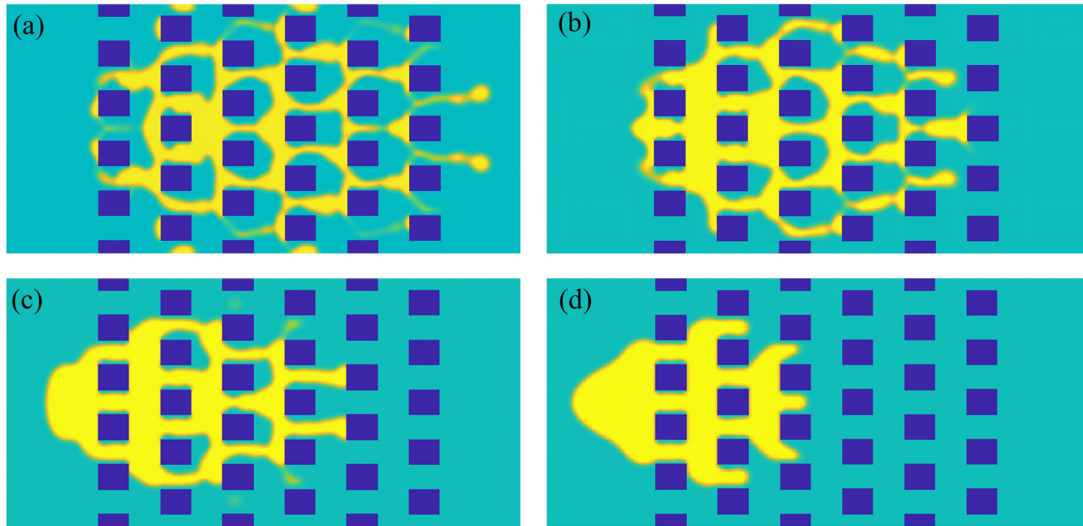


FIG. 13. The liquid and air distributions in the symmetry plane in the vertical direction at $t^* = 1.2$: (a) $\theta = 16.9^\circ$; (b) $\theta = 46.5^\circ$; (c) $\theta = 96.7^\circ$; and (d) $\theta = 131.3^\circ$. The yellow color indicates liquid while the blue colors represents air. The dark blue rectangles stand for the micropillars.

$\cos(\theta)$ indicates a higher $\gamma_{\text{liquid-solid}}$, which finally results in a lower $S_{\text{liquid-solid}}$ and a lower S . In addition, it needs to be noticed that there is no liquid penetration throughout the micropillar for the $\theta = 131.3^\circ$ case.

Figure 13 demonstrates the liquid (yellow color) distribution in the symmetry plane in the vertical direction at $t^* = 1.2$ for various θ cases. In line with the results in Fig. 12, for the lower θ cases, the droplet penetrates faster and spreads wider. It is also noticed that a significant air entrapment can be observed between the liquid and the wall of the micropillar (blue color) for the lower θ cases, which is caused by the higher penetration velocity. This finding has also been observed in the multiphase fluid interaction with the pores structure.^{61,62} It is also found that air entrapment significantly decreases for the higher θ cases, mainly because the lower penetration velocity allows the liquid to slowly fill the gaps between the micropillars, which features a fingering structure.

The evolution of L^* for different θ cases is plotted at Fig. 14(a). As indicated in the figure, the development of L^* is faster for the smaller θ cases, which is the same as the qualitative results in Fig. 12. Similar to the results in Fig. 7(a), the evolution process of L^* during the whole recorded period ($t^* = 0 - 2$) is approximately a linear dependency. The transient evolution of L^* in the first row of micropillars is plotted in the inset of Fig. 14(a). As shown in the figure, the hydrophilic micropillar surface ($\theta \leq 90^\circ$) accelerates the penetration owing to the capillary effect, which results in a higher penetration velocity, while the hydrophobic micropillar surface ($\theta > 90^\circ$) prevents the penetration because of the resistance from the surface tension and leads to a lower penetration velocity. The droplet penetration behavior in the longitudinal direction with different θ also approves our previous analysis in Sec. III A and Eq. (13). For the variation of S^* , as demonstrated in Fig. 14(b), it first increases to a peak value and then decreases slightly, and the maximum value of S^* is increased significantly as θ decreases, which agrees with the results shown in Fig. 12 and the energy analysis.

The evolution of M^* vs t^* is plotted in Fig. 14(c). As seen in the figure, the maximum value of M^* is the lowest for the highest θ case. Furthermore, a higher penetration rate leads to the droplet passing through the micropillar array more quickly. As a result, we can see M^* decreases faster for $\theta \leq 90^\circ$ cases after the infiltration stage [squares and circles in Fig. 14(c)]. Like Figs. 8(b) and 11(b), the transient evolution of penetration mass during the infiltration stage is plotted in Fig. 14(d) with log-log axes. As demonstrated in the figure, the droplet penetration rate follows a power-law dependency and the exponent collapses, which concurs with our previous analysis in Sec. III A. The proposed model [Eq. (17)] is plotted as lines in the figure. As it can be seen, our proposed model is consistent with the simulation results, and the penetration mass for all cases follows a $M^* = Ct^{*1.73}$ dependency. However, due to a higher We ($We \sim 10^1$), the capillary effect plays a negligible role. Therefore, it is noticed that both the theoretical and simulation results of the droplet penetration rate are very close to each other for all θ cases. Additionally, a slightly lower penetration rate is observed for the simulation results at hydrophobic cases ($\theta = 96.7^\circ$ and 131.3°), possibly because the adopted static contact angle model underestimates the capillary resistance when $\theta_f > \pi/2$.

The evolution of droplet penetration mass for all We , ϕ_{la} , and θ cases almost collapse into a t^* to $M^*/(We + 2 \cdot \cos(\theta_f))^{0.5} \cdot \phi_{la}^{0.635}$ relation in Fig. 15. As seen, the modified penetration mass $M^*/(We + 2 \cdot \cos(\theta_f))^{0.5} \cdot \phi_{la}^{0.635}$ agrees well with a $(t/\tau)^{1.73}$ dependency (the dashed line in Fig. 15) for a wide range of t^* . It is noticed that the main deviation occurs at the very early period for various ϕ_{la} cases, which is in line with our finding in Sec. III B. Furthermore, the modified penetration mass for all θ cases is very consistent with each other, which indicates the wettability effect on the penetration rate is not significant for the current situation ($We \sim 10^1$). Nevertheless, it is necessary to investigate the droplet penetrating dynamics for a wider range of surface wettability and impact velocity in future studies.

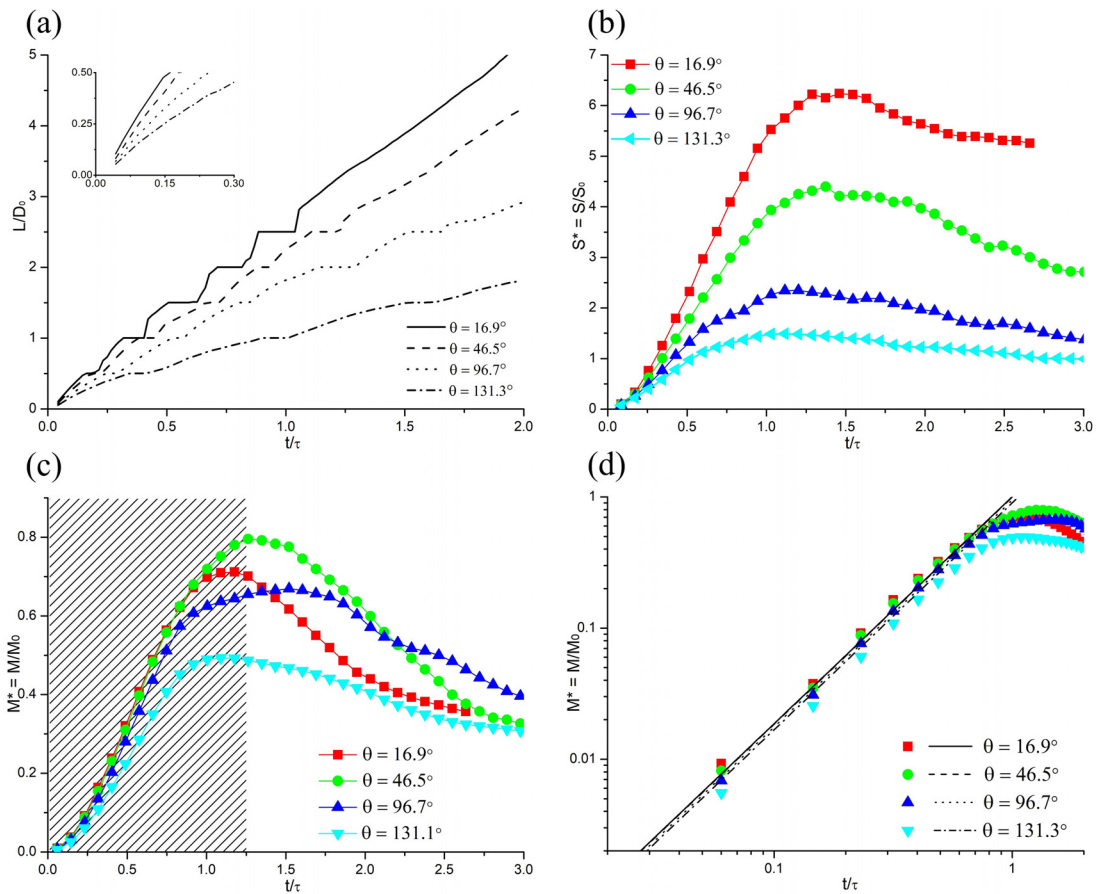


FIG. 14. For the cases of various θ , at $We = 8.3$ and $\phi_{la} = \phi_{lo} = 0.5$. (a) Transient evolution of the penetration length. (b) Transient evolution of the wetted surface area. (c) The variation of the penetration mass during the whole simulation period and (d) the development of the penetration mass during the infiltration stage. Equation (17) is plotted as the lines in (d).

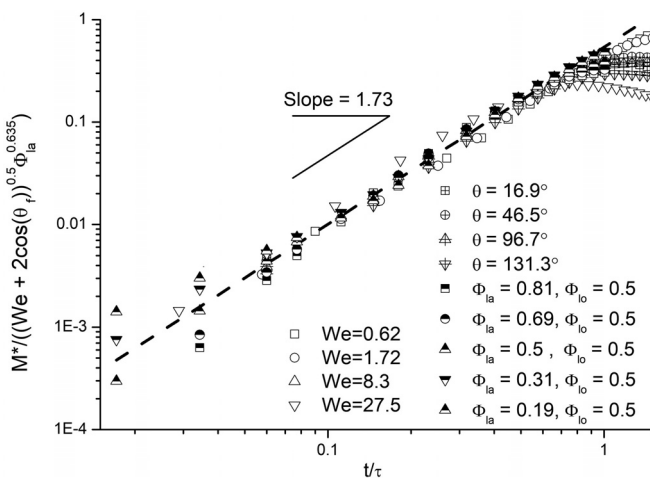


FIG. 15. The modified penetration mass ($M^*/((We + 2 \cdot \cos(\theta_r))^{0.5} \cdot \phi_{la}^{0.635})$) as a function of dimensionless time t/τ . The dashed line in the figure stands for the function $0.54 \cdot (t^*)^{1.73}$.

IV. CONCLUSION

In this study, a nonorthogonal MRT-LB model is applied to simulate a water droplet penetrating a micropillar array in a microchannel. We first quantitatively and qualitatively validate the LB model against experimental results of (a) off-center impact of a water droplet on a single-ridge superhydrophobic surface and (b) impact of a water droplet on a curved superhydrophobic surface. Then, a comprehensive parametric study is carried out to investigate the effects of impacting velocity V_0 , opening fractions of the micropillar array (ϕ_{la} and ϕ_{lo}) as well as the micropillar surface wettability (θ). Based on the results and analysis, we find the droplet dynamics in the longitudinal direction is determined by the competition between the dynamic pressure and the capillary pressure, and the development of the penetration length can be approximated by a linear fitting. The permeation of the droplet is governed by the capillary effect and mainly expands in the vertical directions. For the higher Weber number cases ($We \geq 10^1$), the droplet presents a higher penetration velocity, penetration rate, and maximum wetted surface area (S). For the lower We cases ($We \approx 10^0$), the penetration velocities have no significant differences. Regarding the effects of the opening fractions of the micropillar array, we find a

higher ϕ_{la} leads to a higher droplet penetration velocity, shorter penetration time, and lower maximum S . The shift of ϕ_{lo} has little influence on the droplet penetration time for higher ϕ_{la} cases. Moreover, the penetration rate is decreased with ϕ_{la} , and similar for the cases with the same ϕ_{lo} , which is attributed to the negligible droplet permeation in the lateral direction.

We also find the wettability of the micropillars has a significant effect on the droplet penetration velocity and wetted surface area. Generally, a higher θ results in a much lower penetration velocity and smaller maximum S . For the hydrophilic cases, the droplet penetration velocity is larger, and the liquid penetrates throughout the micropillar array faster compared with the hydrophobic cases. In contrast, the hydrophobic micropillar obviously prevents the penetration of droplets. It is also observed that the penetration rates for all θ cases are close, which may be attributed to the negligible capillary effect in the considered parameter space. According to the precipices of droplet dynamics in the different directions, theoretical models to describe the transient evolution of the dimensionless droplet penetration mass (M^*) are proposed. By comparing the predicted results from the models with the simulations, it is shown that our proposed models work well for a wide range of M^* and t^* , under various V_0 , ϕ_{la} , and θ . For simplicity, the static contact model is adopted in this study, which introduces some limitations in the present model. Therefore, it would be informative to study a wider range of impact velocity and wettability with a dynamic contact angle model in the future.

SUPPLEMENTARY MATERIAL

See the [supplementary material](#) for the supplementary movies.

ACKNOWLEDGMENTS

This work was supported by the UK Engineering and Physical Sciences Research Council (EPSRC) under the project “UK Consortium on Mesoscale Engineering Sciences (UKCOMES)” (Grant No. EP/R029598/1) and the project “Exascale Computing for System-Level Engineering: Design, Optimisation and Resilience” (Grant No. EP/V001531/1).

DATA AVAILABILITY

The data that support the findings of this study are available from the corresponding author upon reasonable request.

REFERENCES

- Y. Peles, A. Koşar, C. Mishra, C. J. Kuo, and B. Schneider, “Forced convective heat transfer across a pin fin micro heat sink,” *Int. J. Heat Mass Transfer* **48**, 3615 (2005).
- L. Zhang, J. M. Koo, L. Jiang, M. Asheghi, K. E. Goodson, J. G. Santiago, and T. W. Kenny, “Measurements and modeling of two-phase flow in microchannels with nearly constant heat flux boundary conditions,” *J. Microelectromech. Syst.* **11**, 12 (2002).
- W. Xing, J. Plawsky, C. Woodcock, X. Yu, A. Ullmann, N. Brauner, and Y. Peles, “Liquid-liquid phase separation heat transfer in advanced micro structure,” *Int. J. Heat Mass Transfer* **127**, 989 (2018).
- X. Casadevall i Solvas and A. De Mello, “Droplet microfluidics: Recent developments and future applications,” *Chem. Commun.* **47**, 1936 (2011).
- C. Chung, M. Lee, K. Char, K. H. Ahn, and S. J. Lee, “Droplet dynamics passing through obstructions in confined microchannel flow,” *Microfluid. Nanofluid.* **9**, 1151 (2010).
- J. Linan, W. Man, and Z. Yitshak, “Forced convection boiling in a microchannel heat sink,” *J. Microelectromech. Syst.* **10**, 80 (2001).
- W. Qu and I. Mudawar, “Flow boiling heat transfer in two-phase micro-channel heat sinks-I. Experimental investigation and assessment of correlation methods,” *Int. J. Heat Mass Transfer* **46**, 2755 (2003).
- X. Yu, J. Xu, J. Yuan, and W. Zhang, “Microscale phase separation condensers with varied cross sections of each fluid phase: Heat transfer enhancement and pressure drop reduction,” *Int. J. Heat Mass Transfer* **118**, 439 (2018).
- Y. N. Cheung, N. T. Nguyen, and T. N. Wong, “Low-frequency acoustic atomization with oscillatory flow around micropillars in a microfluidic device,” *Appl. Phys. Lett.* **105**, 144103 (2014).
- S. M. Kim and I. Mudawar, “Thermal design and operational limits of two-phase micro-channel heat sinks,” *Int. J. Heat Mass Transfer* **106**, 861 (2017).
- D. R. Link, S. L. Anna, D. A. Weitz, and H. A. Stone, “Geometrically mediated breakup of drops in microfluidic devices,” *Phys. Rev. Lett.* **92**, 054503 (2004).
- K. Akamatsu, K. Minezaki, M. Yamada, M. Seki, and S. I. Nakao, “Direct observation of splitting in oil-in-water-in-oil emulsion droplets via a microchannel mimicking membrane pores,” *Langmuir* **33**, 14087 (2017).
- L. Salkin, L. Courbin, and P. Panizza, “Microfluidic breakups of confined droplets against a linear obstacle: The importance of the viscosity contrast,” *Phys. Rev. E* **86**, 036317 (2012).
- X. Niu, S. Gulati, J. B. Edel, and A. J. Demello, “Pillar-induced droplet merging in microfluidic circuits,” *Lab Chip* **8**, 1837 (2008).
- Q. Li, Z. Chai, B. Shi, and H. Liang, “Deformation and breakup of a liquid droplet past a solid circular cylinder: A lattice Boltzmann study,” *Phys. Rev. E* **90**, 043015 (2014).
- S. Bhardwaj, A. Dalal, G. Biswas, and P. P. Mukherjee, “Analysis of droplet dynamics in a partially obstructed confinement in a three-dimensional channel,” *Phys. Fluids* **30**, 102102 (2018).
- H. L. Li, H. R. Liu, and H. Ding, “A fully 3D simulation of fluid-structure interaction with dynamic wetting and contact angle hysteresis,” *J. Comput. Phys.* **420**, 109709 (2020).
- C. Chung, K. H. Ahn, and S. J. Lee, “Numerical study on the dynamics of droplet passing through a cylinder obstruction in confined microchannel flow,” *J. Non-Newtonian Fluid Mech.* **162**, 38 (2009).
- Y. Ma, M. Zheng, M. G. Bah, and J. Wang, “Effects of obstacle lengths on the asymmetric breakup of a droplet in a straight microchannel,” *Chem. Eng. Sci.* **179**, 104 (2018).
- W. Lee and G. Son, “Numerical study of obstacle configuration for droplet splitting in a microchannel,” *Comput. Fluids* **84**, 351 (2013).
- H. Chen, J. Zhang, Y. Zhang, and Z. Wei, “Simulation on a gravity-driven dripping of droplet into micro-channels using the lattice Boltzmann method,” *Int. J. Heat Mass Transfer* **126**, 61 (2018).
- Q. Li, K. H. Luo, Q. J. Kang, Y. L. He, Q. Chen, and Q. Liu, “Lattice Boltzmann methods for multiphase flow and phase-change heat transfer,” *Prog. Energy Combust. Sci.* **52**, 62 (2016).
- S. Chen and G. D. Doolen, “Lattice Boltzmann method for fluid flows,” *Annu. Rev. Fluid Mech.* **30**, 329 (1998).
- L. Chen, Q. Kang, Y. Mu, Y. L. He, and W. Q. Tao, “A critical review of the pseudopotential multiphase lattice Boltzmann model: Methods and applications,” *Int. J. Heat Mass Transfer* **76**, 210 (2014).
- Q. Li, K. H. Luo, and X. J. Li, “Lattice Boltzmann modeling of multiphase flows at large density ratio with an improved pseudopotential model,” *Phys. Rev. E* **87**, 053301 (2013).
- X. Shan and H. Chen, “Lattice Boltzmann model for simulating flows with multiple phases and components,” *Phys. Rev. E* **47**, 1815 (1993).
- H. Huang, D. T. Thorne, M. G. Schaap, and M. C. Sukop, “Proposed approximation for contact angles in Shan-and-Chen-type multicomponent multiphase lattice Boltzmann models,” *Phys. Rev. E* **76**, 066701 (2007).
- Q. Li, K. H. Luo, Q. J. Kang, and Q. Chen, “Contact angles in the pseudopotential lattice Boltzmann modeling of wetting,” *Phys. Rev. E* **90**, 053301 (2014).
- H. Huang, M. C. Sukop, and X. Y. Lu, *Multiphase Lattice Boltzmann Methods: Theory and Application* (Wiley Blackwell, 2015).
- L. Fei, J. Du, K. H. Luo, S. Succi, M. Lauricella, A. Montessori, and Q. Wang, “Modeling realistic multiphase flows using a non-orthogonal multiple-relaxation-time lattice Boltzmann method,” *Phys. Fluids* **31**, 042105 (2019).
- Q. Li and K. H. Luo, “Achieving tunable surface tension in the pseudopotential lattice Boltzmann modeling of multiphase flows,” *Phys. Rev. E* **88**, 053307 (2013).

- ³²Z. Guo, C. Zheng, and B. Shi, "Discrete lattice effects on the forcing term in the lattice Boltzmann method," *Phys. Rev. E* **65**, 046308 (2002).
- ³³L. Fei and K. H. Luo, "Consistent forcing scheme in the cascaded lattice Boltzmann method," *Phys. Rev. E* **96**, 053307 (2017).
- ³⁴P. Yuan and L. Schaefer, "Equations of state in a lattice Boltzmann model," *Phys. Fluids* **18**, 042101 (2006).
- ³⁵C. E. Colosqui, G. Falcucci, S. Ubertini, and S. Succi, "Mesoscopic simulation of non-ideal fluids with self-tuning of the equation of state," *Soft Matter* **8**, 3798 (2012).
- ³⁶J. Yang, X. Ma, L. Fei, X. Zhang, K. H. Luo, and S. Shuai, "Effects of hysteresis window on contact angle hysteresis behaviour at large bond number," *J. Colloid Interface Sci.* **566**, 327 (2020).
- ³⁷L. Wang, H. B. Huang, and X. Y. Lu, "Scheme for contact angle and its hysteresis in a multiphase lattice Boltzmann method," *Phys. Rev. E* **87**, 013301 (2013).
- ³⁸D. Lycett-Brown and K. H. Luo, "Multiphase cascaded lattice Boltzmann method," *Comput. Math. Appl.* **67**, 350 (2014).
- ³⁹Q. Li, D. H. Du, L. L. Fei, and K. H. Luo, "Three-dimensional non-orthogonal MRT pseudopotential lattice Boltzmann model for multiphase flows," *Comput. Fluids* **186**, 128 (2019).
- ⁴⁰L. Fei, K. H. Luo, and Q. Li, "Three-dimensional cascaded lattice Boltzmann method: Improved implementation and consistent forcing scheme," *Phys. Rev. E* **97**, 053309 (2018).
- ⁴¹G. Wang, L. Fei, and K. H. Luo, "Lattice Boltzmann simulation of water droplet impacting a hydrophobic plate with a cylindrical pore," *Phys. Rev. Fluids* **5**, 83602 (2020).
- ⁴²G. Wang, J. Gao, and K. H. Luo, "Droplet impacting a superhydrophobic mesh array: Effect of liquid properties," *Phys. Rev. Fluids* **5**, 123605 (2020).
- ⁴³J. C. Bird, S. Mandre, and H. A. Stone, "Short-time dynamics of partial wetting," *Phys. Rev. Lett.* **100**, 234501 (2008).
- ⁴⁴Z. Hu, X. Wu, F. Chu, X. Zhang, and Z. Yuan, "Off-centered droplet impact on single-ridge superhydrophobic surfaces," *Exp. Therm. Fluid Sci.* **120**, 110245 (2021).
- ⁴⁵Y. Liu, M. Andrew, J. Li, J. M. Yeomans, and Z. Wang, "Symmetry breaking in drop bouncing on curved surfaces," *Nat. Commun.* **6**, 10034 (2015).
- ⁴⁶P.-G. De Gennes, F. Brochard-Wyart, and D. Quéré, *Capillarity and Wetting Phenomena: Drops, Bubbles, Pearls, Waves* (Springer Science & Business Media, 2013).
- ⁴⁷D. Soto, H. L. Girard, A. Le Helloco, T. Binder, D. Quéré, and K. K. Varanasi, "Droplet fragmentation using a mesh," *Phys. Rev. Fluids* **3**, 083602 (2018).
- ⁴⁸S. Ding, X. Liu, X. Wu, and X. Zhang, "Droplet breakup and rebound during impact on small cylindrical superhydrophobic targets," *Phys. Fluids* **32**, 102106 (2020).
- ⁴⁹H. Ding and T. G. Theofanous, "The inertial regime of drop impact on an anisotropic porous substrate," *J. Fluid Mech.* **691**, 546 (2012).
- ⁵⁰D. Quéré, "Inertial capillarity," *Europhys. Lett.* **39**, 533 (1997).
- ⁵¹A. Delbos, E. Lorenceau, and O. Pitois, "Forced impregnation of a capillary tube with drop impact," *J. Colloid Interface Sci.* **341**, 171 (2010).
- ⁵²S. Das, H. V. Patel, E. Milacic, N. G. Deen, and J. A. M. M. Kuipers, "Droplet spreading and capillary imbibition in a porous medium: A coupled IB-VOF method based numerical study," *Phys. Fluids* **30**, 012112 (2018).
- ⁵³P. Vaitukaitis, D. Maggiolo, J. Rimmelgas, S. Abrahamsen-Alami, D. Bernin, M. Siiskonen, J. Malmqvist, S. Sasic, and G. Sardina, "Water transport and absorption in pharmaceutical tablets – A numerical study," *Meccanica* **55**, 421 (2020).
- ⁵⁴A. Kumar, A. Tripathy, Y. Nam, C. Lee, and P. Sen, "Effect of geometrical parameters on rebound of impacting droplets on leaky superhydrophobic meshes," *Soft Matter* **14**, 1571 (2018).
- ⁵⁵D. J. Bouchard and S. Chandra, "Droplet impact and flow into a gap between parallel plates," *Phys. Fluids* **31**, 062104 (2019).
- ⁵⁶R. G. Cox, "The dynamics of the spreading of liquids on a solid surface. Part 2. Surfactants," *J. Fluid Mech.* **168**, 195 (1986).
- ⁵⁷W. Gardner, "Note on the dynamics of capillary flow," *Phys. Rev.* **18**, 206 (1921).
- ⁵⁸J. Cai and B. Yu, "A discussion of the effect of tortuosity on the capillary imbibition in porous media," *Transp. Porous Media* **89**, 251 (2011).
- ⁵⁹R. L. Hoffman, "A study of the advancing interface. I. Interface shape in liquid-gas systems," *J. Colloid Interface Sci.* **50**, 228 (1975).
- ⁶⁰K. G. Winkels, J. H. Wejjs, A. Eddi, and J. H. Snoeijer, "Initial spreading of low-viscosity drops on partially wetting surfaces," *Phys. Rev. E* **85**, 055301(R) (2012).
- ⁶¹A. O'Brien, S. Afkhami, and M. Bussmann, "Pore-scale direct numerical simulation of Haines jumps in a porous media model," *Eur. Phys. J.: Spec. Top.* **229**, 1785 (2020).
- ⁶²L. Cueto-Felgueroso, X. Fu, and R. Juanes, "Pore-scale modeling of phase change in porous media," *Phys. Rev. Fluids* **3**, 084302 (2018).